

Frontogenesis, Mixing, and Stratification in Estuarine Channels with Curvature

TONG BO^{a,b} AND DAVID K. RALSTON^a

^a *Applied Ocean Physics and Engineering Department, Woods Hole Oceanographic Institution, Woods Hole, Massachusetts*

^b *MIT-WHOI Joint Program in Oceanography/Applied Ocean Science and Engineering, Cambridge, Massachusetts*

(Manuscript received 3 December 2021, in final form 14 February 2022)

ABSTRACT: Idealized numerical simulations were conducted to investigate the influence of channel curvature on estuarine stratification and mixing. Stratification is decreased and tidal energy dissipation is increased in sinuous estuaries compared to straight channel estuaries. We applied a vertical salinity variance budget to quantify the influence of straining and mixing on stratification. Secondary circulation due to the channel curvature is found to affect stratification in sinuous channels through both lateral straining and enhanced vertical mixing. Alternating negative and positive lateral straining occur in meanders upstream and downstream of the bend apex, respectively, corresponding to the normal and reversed secondary circulation with curvature. The vertical mixing is locally enhanced in curved channels with the maximum mixing located upstream of the bend apex. Bend-scale bottom salinity fronts are generated near the inner bank upstream of the bend apex as a result of interaction between the secondary flow and stratification. Shear mixing at bottom fronts, instead of overturning mixing by the secondary circulation, provides the dominant mechanism for destruction of stratification. Channel curvature can also lead to increased drag, and using a Simpson number with this increased drag coefficient can relate the decrease in stratification with curvature to the broader estuarine parameter space.

KEYWORDS: Estuaries; Mixing; Secondary circulation; Fronts; Tides; Numerical analysis/modeling

1. Introduction

Stratification is a key characteristic of estuaries. Stratification affects the along-estuary transport of salinity and other scalars, and it provides a control on the intensity of vertical mixing and thus influences the vertical distribution of momentum, sediment, chemicals, and biota (Simpson et al. 1990; Geyer and Ralston 2011). Salinity stratification appears in estuaries due to the buoyancy input of freshwater as the influence of gravity tilts horizontal salinity gradients into the vertical direction (e.g., Geyer and Ralston 2011). While estuarine stratification typically depends on the strength of freshwater input and tidal forcing, geomorphic features also affect vertical mixing and stratification, e.g., shallow shoals (Ralston and Stacey 2005b; Geyer et al. 2020), sills (Farmer and Smith 1980; Seim and Gregg 1997), constrictions (Armi and Farmer 1986; Geyer et al. 2017), and channel curvature (Seim and Gregg 1997; Becherer et al. 2015).

Many estuaries have sinuous channels (e.g., Marani et al. 2002; Fagherazzi et al. 2004), and the channel curvature can lead to distinct hydrodynamic processes including the development of secondary circulation (e.g., Thomson 1877; Rozovskii 1957) and flow separation (e.g., Leopold 1960; Leeder and Bridges 1975). In curved open-channel flows, secondary circulation arises in a lateral plane perpendicular to the main flow as a result of the local imbalance between the centrifugal acceleration and barotropic pressure gradient (e.g., Thomson 1877). Curvature-induced secondary circulation has been observed in rivers (e.g., Apmann 1964) and estuaries (e.g., Seim and Gregg 1997; Chant and Wilson 1997), typically with flow toward the outer bank near the surface and toward the inner bank in the lower layer. However, in estuaries salinity

stratification can alter the effect of curvature on the flow. Stratification can enhance the shear of the streamwise flow and thereby strengthen the secondary circulation (Geyer 1993b). Alternatively, lateral baroclinic pressure gradients can reverse the sense of lateral circulation or lead to multiple circulation cells and more complex structure than in homogeneous density flow (Chant and Wilson 1997; Lacy and Monismith 2001; Nidziko et al. 2009; Scully et al. 2009; Kranenburg et al. 2019). In addition to secondary circulation, flow separation can affect the velocity distribution in sinuous channels, with streamlines of the main flow detaching from the inner bank and recirculating eddies in the lee of bends (e.g., Leopold 1960; Leeder and Bridges 1975).

In sinuous estuarine channels, the curvature-induced secondary circulation can reduce stratification by enhancing vertical mixing. Secondary circulation was found to reduce stratification in a curved channel in Puget Sound by laterally overturning the water column and generating intense mixing (Seim and Gregg 1997). In that study, a bend Froude number was introduced to compare the overturning and mixing due to curvature with the stratification that suppresses overturning. In Elkhorn Slough, a shallow, sinuous salt marsh estuary, the bend Froude number was found to be below the criterion for overturning to occur, and instead, shear-generated turbulence was dominant in mixing (Nidziko et al. 2009). Meanders were also found to enhance turbulent mixing in an idealized modeling study of the Ems estuary, although the detailed mechanism was not reported (Pein et al. 2018).

Frontogenesis is an important process that affects stratification and mixing in estuaries. Estuarine fronts can increase the streamwise baroclinic pressure gradient, locally enhancing shear of the streamwise flow and leading to intense mixing (Simpson and Linden 1989; Geyer and Ralston 2015; Warner et al. 2020). Typical examples of estuarine salinity fronts

Corresponding author: Tong Bo, tongbo@mit.edu

DOI: 10.1175/JPO-D-21-0298.1

© 2022 American Meteorological Society. For information regarding reuse of this content and general copyright information, consult the AMS Copyright Policy (www.ametsoc.org/PUBSReuseLicenses).

TABLE 1. Geometric parameters and tidal and discharge conditions of all the sharp-bend, smooth-bend, and straight channel models. The models selected for detailed analysis are marked with stars; R is the bend radius of curvature, H is the thalweg depth of the focus region, and W is the channel width.

Model	R (m)	H (m)	W (m)	R/W	Tidal range (m)	River discharge ($\text{m}^3 \text{s}^{-1}$)
sharp1★	50	4	60	0.8	2.0	1.5
sharp2	50	4	60	0.8	1.6	1.5
sharp3	50	6	60	0.8	2.0	7.5
sharp4	50	6	60	0.8	2.4	7.5
smooth1★	120	4	60	2	2.0	1.5
smooth2	120	4	60	2	1.6	1.5
smooth3	120	6	60	2	2.0	7.5
smooth4	120	6	60	2	2.4	7.5
straight1★	—	4	60	—	2.0	1.5
straight2	—	4	60	—	1.6	1.5
straight3	—	6	60	—	2.0	7.5
straight4	—	6	60	—	2.4	7.5

include, e.g., tidal intrusion fronts (Simpson and Nunes 1981), river plume fronts (Garvine 1974), and bottom fronts associated with constrictions (Geyer and Ralston 2015). Salinity fronts result from interactions between the three-dimensional flow and salinity gradients (Geyer and Ralston 2015). Channel curvature can generate strong lateral velocities as well as lateral variations in salinity and streamwise momentum, and the interactions between the velocity and salinity distributions with flow curvature may provide rich additional means for frontogenesis.

In addition to frontogenesis, interactions between lateral velocities and lateral salinity gradients with flow curvature can affect stratification through the process of lateral straining. In straight channels, differential along-channel advection due to lateral bathymetric variations can create lateral salinity gradients, leading to lateral baroclinic circulation, positive lateral straining, and creation of stratification (e.g., Nunes and Simpson 1985; Lacy et al. 2003; Ralston and Stacey 2005a). However, in sinuous channels, the lateral circulation is not necessarily driven by the lateral salinity gradient since the lateral momentum balance depends on the centrifugal forcing due to channel curvature. As a result, lateral straining with curvature can be either positive or negative, either creating or destroying stratification. In a curved tidal channel in the Wadden Sea, the centrifugal forcing was found to be comparable to the baroclinic forcing in generating lateral circulation and lateral straining, but the tidal asymmetry in the sign of the curvature influence resulted in net positive lateral straining (Becherer et al. 2015). Flow separation at bends can also affect lateral straining by enhancing differential advection and generating secondary circulation that has positive lateral straining (Bo and Ralston 2020).

In this study, we build idealized models to investigate the influence of channel curvature on stratification. Straight and sinuous channel estuaries are compared, with geometric parameters and forcing conditions scaled off a shallow, sinuous estuarine channel with previous observations (Kranenburg et al. 2019; Bo et al. 2021). In section 2, we introduce the numerical models. In section 3, we show the hydrodynamic and stratification conditions in straight and sinuous channels,

including the vertical salinity variance budget that is used to quantify the influences of straining and mixing on stratification. In section 4, we analyze the generation of curvature-induced bottom fronts and its role in enhancing mixing in meanders. We also introduce in an adjusted Simpson number scaling that accounts for the increased drag with channel curvature and parameterizes the decrease in stratification. Section 5 has discussion on the influence of curvature-induced bottom fronts and other mechanisms affecting stratification and mixing in sinuous channels. Section 6 presents conclusions.

2. Methods

Model simulations were conducted using the Regional Ocean Modeling System (ROMS) (Shchepetkin and McWilliams 2005; Haidvogel et al. 2008; Warner et al. 2008, 2010), a 3D hydrostatic model based on the Reynolds-averaged Navier–Stokes (RANS) equations. Twelve estuary models were built that have different channel shapes, channel depths, tides, and river discharges (Table 1) to investigate the influence of channel curvature, channel depth, and forcing conditions on stratification. The sinuous channel shape is inspired by the North River estuary (Massachusetts) (Kranenburg et al. 2019; Bo et al. 2021), a sinuous tidal channel with variable stratification in previous observations. Channel dimensions, tidal conditions, and river discharges are also scaled off conditions in the North River estuary. The channel has a 40-km total length, and it exponentially converges landwards (e.g., Langbein 1963) from the mouth to around 6 km into the estuary, and farther landward the channel width is uniform ($W = 60$ m). The model analysis focuses on the midestuary region at around 12–14 km, which is in the middle of the salinity gradient and away from the river and ocean boundary conditions. Models with three different channel plan forms were compared (Fig. 1a): a straight channel, a sinuous channel with five smooth bends, and a sinuous channel with nine sharp bends, which have the same cross-channel geometry and tidal and discharge conditions. The sinuous channel shape is created following the form of sine-generated functions (Langbein and Leopold 1970). The bend sharpness is quantified by the

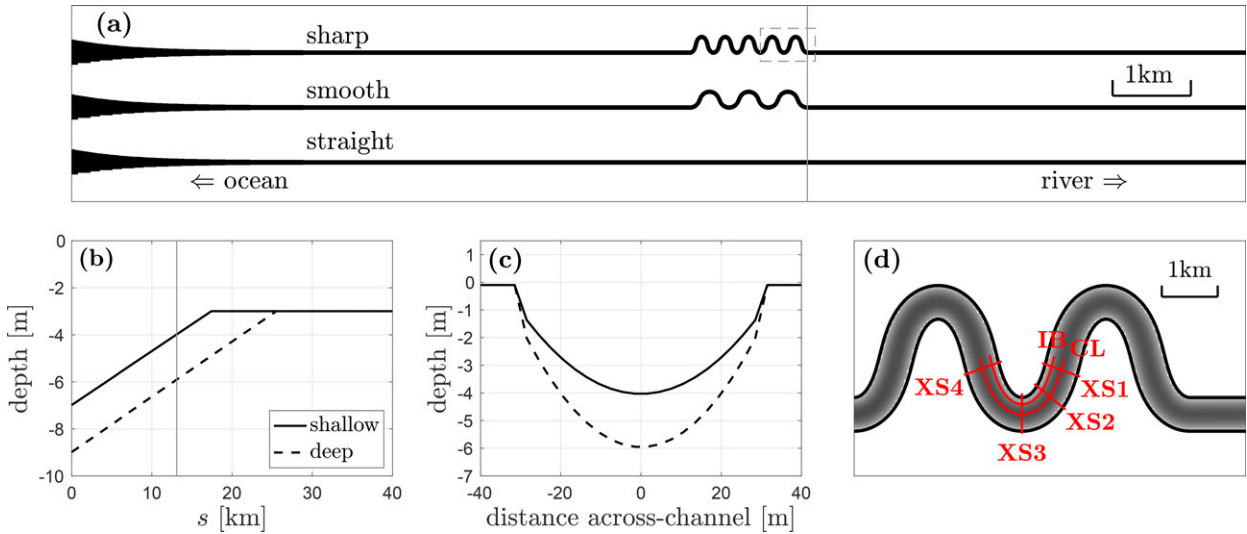


FIG. 1. (a) The sharp-bend, smooth-bend, and straight channel estuary models. The ocean is on the left side. (b) The channel thalweg depth as a function of the along-channel distance s . The solid line shows the shallow channel model and dashed line shows the deep channel model. (c) Cross-sectional bathymetry at $s = 13$ km, corresponding to the cross section denoted by the thin gray lines in (a) and (b). (d) The up-estuary part of the meander region of the sharp-bend model, as is denoted by the dashed rectangle in (a). Red lines show the cross sections (XS1–XS4) and along-channel sections (CL and IB) analyzed in the following sections.

curvature ratio R/W (bend radius of curvature to width ratio), and R/W is 0.8 for the sharp-bend channel and 2.0 for the smooth-bend channel. The bend sharpness of the models is consistent with the North River estuary, i.e., $R/W \sim 1$ for sharp bends and $R/W \sim 2\text{--}4$ for smooth bends (Bo et al. 2021), and is similar to the typical range of $R/W \sim 1\text{--}5$ found in river meanders (Leopold and Wolman 1960) and tidal meanders (Marani et al. 2002). The channel thalweg depth linearly decreases from the mouth to ~ 20 km, and is a uniform 3 m after that (Fig. 1b). A shallow and a deep channel were built for each channel planform to explore the parameter space, with thalweg depths H of 4 and 6 m, respectively, in the focus region. The channel has a parabolic cross section (e.g., Smith 1982) with a minimum depth of 1.5–2 m near the banks (Fig. 1c).

The models are forced by semidiurnal tides on the open ocean boundary. Tidal ranges of 1.6, 2.0, and 2.4 m (Table 1) correspond to maximum tidal currents of 0.5–0.8 m s^{-1} in the focus region. Constant river discharges of 1.5 and 7.5 $\text{m}^3 \text{s}^{-1}$ input at the landward boundary (Table 1) correspond to mean velocities of 1 and 5 cm s^{-1} in the focus region. The models have constant salinity of 32 psu at the ocean boundary and 0 psu at the river boundary. Temperature is constant and uniform throughout the domain. The model was run to a periodic (semidiurnal) steady state. The analysis primarily focuses on the sharp-bend, smooth-bend, and straight channel models with the shallow thalweg depth, 2-m range tides, and 1.5 $\text{m}^3 \text{s}^{-1}$ discharge, which corresponds with common conditions of intermediate tides and low discharge in the North River estuary.

The model grids are structured, with 3-m resolution in the focused region, i.e., around 20 grid cells across the 60-m-wide channel, and grid spacing increases toward the boundaries. A terrain-following coordinate with 16 uniformly distributed layers is used in the vertical direction. The generic length

scale (GLS) mixing scheme is used for the vertical turbulent mixing (Umlauf and Burchard 2003; Warner et al. 2005) and the horizontal mixing coefficient K_H is set to 0.01 $\text{m}^2 \text{s}^{-1}$. In addition, numerical mixing is assessed following the approach of (Burchard and Rennau 2008). Numerical mixing arises from discretization errors of the tracer advection scheme, and can be calculated as the difference between the advected square of the tracer and the square of advected tracer (e.g., Burchard and Rennau 2008; Ralston et al. 2017; Kalra et al. 2019). Bottom roughness z_0 is 0.002 m, a typical value for a bed with ripples (Grant and Madsen 1982). The Coriolis force is included in the models. While the Coriolis effect could be crucial for estuarine salinity dynamics (e.g., Valle-Levinson 2008; Scully et al. 2009; Valle-Levinson 2011), it is negligible in the narrow estuaries investigated in the present study.

3. Results

In this section, we compare sinuous and straight channel models to investigate the influence of channel curvature on the flow field and salinity stratification. In section 3a, the general features of tides and salinity field are compared. In section 3b, we examine the curvature-induced secondary circulation and its impact on salinity distribution in the channel bend. In section 3c, we apply the vertical salinity variance budget analysis to investigate straining, mixing, and their influences on stratification in the sinuous and straight channel models.

a. Tides and stratification

Comparison of the sharp-bend, smooth-bend, and straight channel models illustrates the influence of channel curvature on tidal amplitude and stratification (Fig. 2). The models have

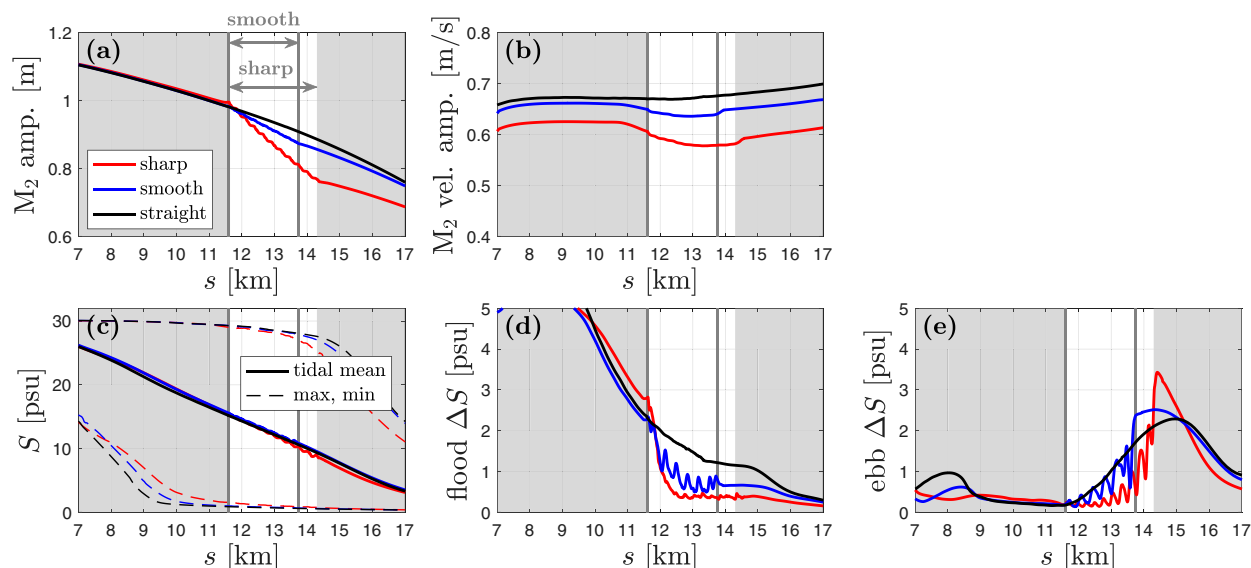


FIG. 2. Along-channel change of tides and salinity in the sharp-bend, smooth-bend, and straight models with shallow depth, 2-m tidal range, and $1.5 \text{ m}^3 \text{ s}^{-1}$ discharge. The white background shows the range of sharp bends, and the vertical gray lines show the range of smooth bends. (a) M_2 tidal amplitude. See legends for details. M_2 amplitude is 1 m on the ocean boundaries. (b) M_2 velocity amplitude. (c) Tidal mean salinity (solid lines) and maximum/minimum salinity (dashed lines). (d), (e) Mean stratification during flood and ebb tides, respectively. Stratification is quantified as the bottom-surface salinity difference ΔS .

the same tidal and river boundary conditions, channel depth, and channel shape except for the sinuous region at around 12–14 km. The three models have 1-m amplitude (2-m range) M_2 tides imposed on the ocean boundaries, and the M_2 tidal amplitude increases inside the estuary mouth because of channel convergence. Landward of around 6 km, channel width becomes uniform and M_2 amplitude decays due to drag (Fig. 2a). Tidal amplitude decays more rapidly in the meander regions of the sinuous models because channel curvature increases the drag through enhanced bottom friction and additional form drag around bends (e.g., Leopold 1960; Chang 1984; Bo and Ralston 2020). Tidal amplitude decays faster in the sharp-bend model than the smooth-bend model because greater drag is expected for stronger channel curvature (e.g., James 1994; Bo and Ralston 2020). The M_2 velocity amplitude is decreased in sinuous models compared to the straight model (Fig. 2b), because of the reduction in tidal amplitude with channel curvature.

The mean along-channel salinity distribution is similar among the three models (Fig. 2c). The tidal excursion is around 10 km in the straight channel model, and is 0.5–1 km shorter in the sinuous models, which can be explained by the decreased tidal currents due to the meanders. The tidal excursion is comparable to the salinity intrusion length, and is much longer than the topographic features of interest, i.e., channel bends, which is common for short estuaries like the North River (Garcia et al. 2021). The salinity intrusion propagates landward of the meander region (12–14 km) during flood tide, and retreats seaward of the meanders during ebb.

All of the channel configurations illustrated here are periodically stratified. Stratification is created near the estuary

mouth and advected landward to ~ 15 km during flood tide and disappears after maximum flood. Likewise, during early ebb tide stratification appears landward of the meander region and moves seaward until being completely mixed by maximum ebb tide. The sinuous models are generally less stratified than the straight channel during both flood and ebb tides, and stratification is weaker in the sharp-bend model than the smooth-bend model (Figs. 2d,e). While the weaker tidal current in sinuous channels (Fig. 2b) is expected to lead to weaker tidal mixing and stronger stratification, stratification instead decreases through the meander region, indicating that channel curvature can decrease stratification. Moreover, the sinuous models are less stratified than the straight model landward of the meanders during flood tide, which implies the nonlocal influence of meanders in decreasing stratification. During ebb tide, stratification landward of the meanders is slightly stronger than the straight model due to the relatively weaker tides in the sinuous cases (Figs. 2a,b). Comparison of the three models suggests that channel curvature generally reduces stratification, and the underlying mechanisms will be investigated in the following section. In addition to the example cases, model results across the range of forcing conditions and channel depths consistently demonstrate the influence of channel curvature in decreasing stratification. For example, the case with a deeper channel and stronger river discharge is permanently stratified as a straight channel but has tidally periodic stratification in both cases with curvature.

b. Secondary circulation and salinity distribution

During ebb tides, secondary circulation is observed in the meander region of all the sinuous models, and here we take

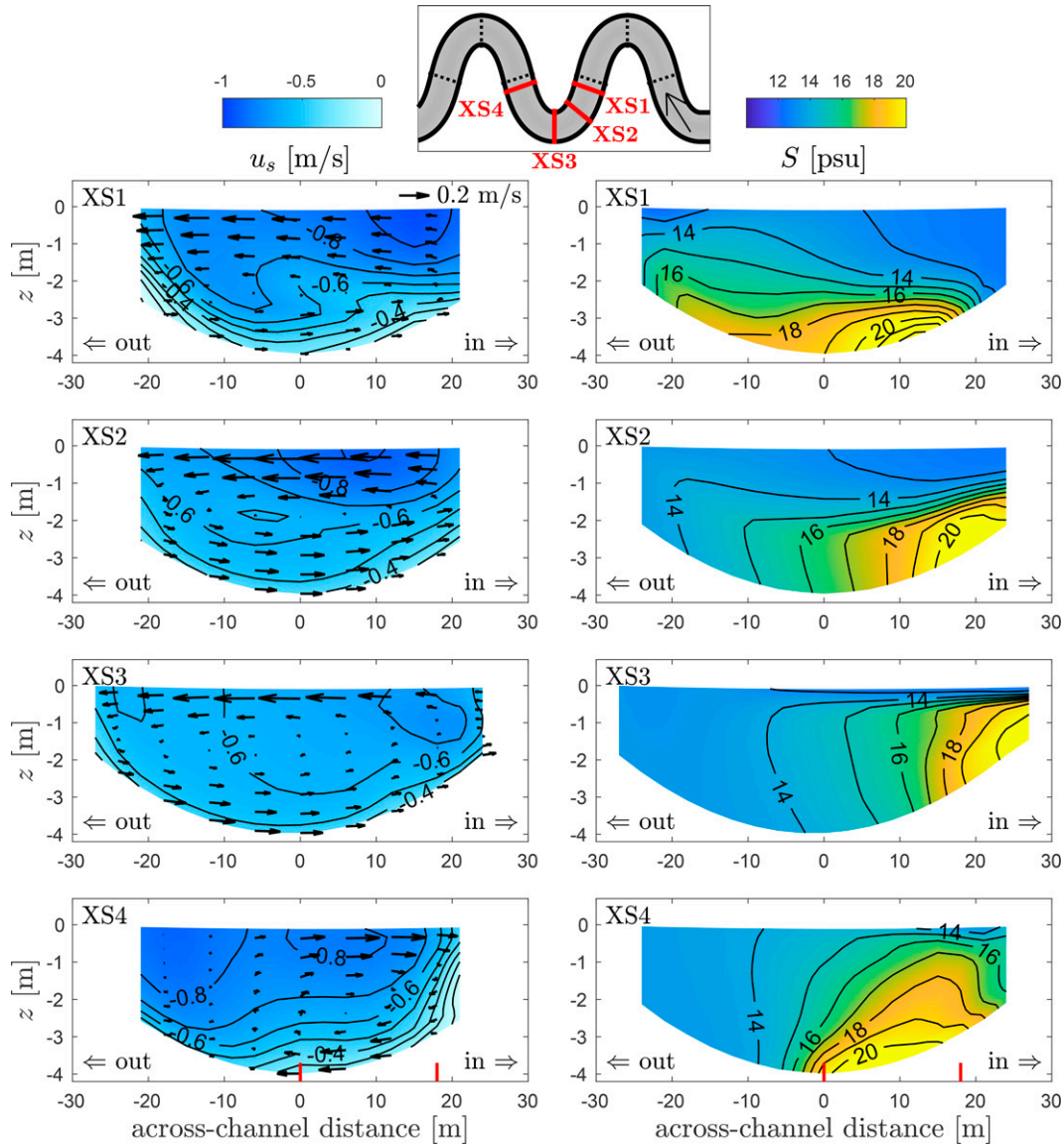


FIG. 3. Streamwise velocity (left) u_s and (right) salinity S in four cross sections in a bend at 2 h into ebb tide. Negative streamwise velocity means seaward flow. Black arrows show the secondary circulation. The inner bank is on the right side, and outer bank is on the left side in all panels. In the small panel at the top, red lines show locations of the four cross sections, and dotted black lines represent the bend apexes and crossovers. Red vertical lines in the lowest panels show locations of the along-channel sections (CL, IB) in Fig. 4.

one example from the sharp bend model with shallow thalweg depth, 2-m range tides, and $1.5 \text{ m}^3 \text{ s}^{-1}$ discharge. The “normal” secondary circulation due to flow curvature develops in the cross sections from the bend entrance to the apex, with the lateral flow toward the outer bank near the surface and toward the inner bank near the channel bed (Fig. 3, XS1, XS2, XS3). As a result, as the stratified flow enters the bend, the downward vertical velocity near the outer bank advects fresher water with relatively high streamwise momentum from the surface toward the lower layer and squeezes isohalines closer to the bed (Fig. 3, XS1). Correspondingly near the inner bank, as flow approaches the bend apex the halocline

is lifted by the upwelling that is fed by inward flow of high-salinity water near the bed. High-salinity water builds up near the inner bank at the apex (Fig. 3, XS3), and stratification almost disappears because secondary circulation has transformed the vertical salinity gradient coming into the bend into a lateral gradient at the apex.

Downstream of the bend apex, the sense of lateral circulation is reversed because the lateral baroclinic forcing from the lateral salinity gradient becomes greater than the centrifugal forcing, resulting in inward flow near the surface and outward flow near the bottom (Fig. 3, XS4). Consequently, the lateral salinity gradient is converted back to a vertical gradient

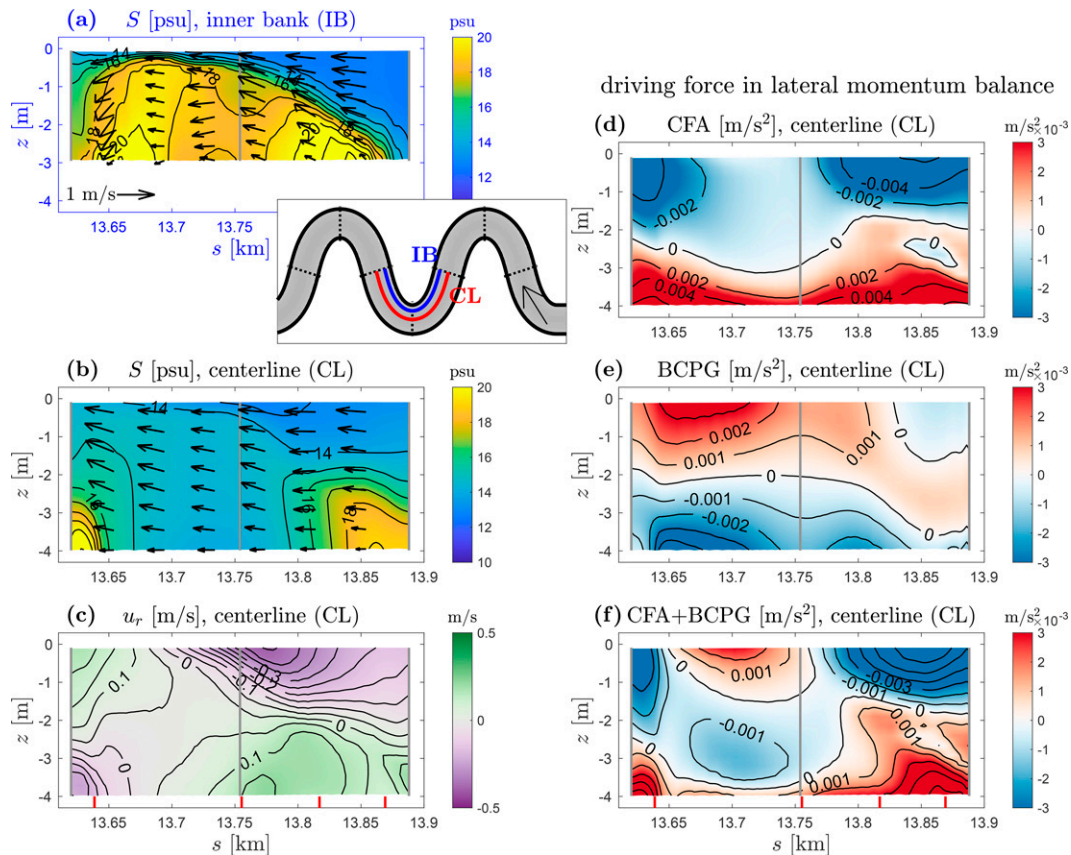


FIG. 4. Along-channel sections in a bend at 2 h into ebb tide. (a) Salinity in an along-channel section near the inner bank (18 m from the centerline). Black arrows show the streamwise and vertical velocities. The bend apex is marked by the gray line at around $s = 13.75$ km. (b) Salinity along the centerline. (c) Lateral velocity u_r along the centerline. The positive direction is inward and negative direction is outward. (d)–(f) Driving force in the lateral momentum balance (centrifugal acceleration CFA, baroclinic pressure gradient force BCPG, and CFA + BCPG). Positive values represent inward forcing. In the small panel, for (a), the blue line shows the section along the inner bank [IB, for (a)], and the red line shows centerline (CL, for all other panels). Dotted black lines represent the bend apexes and crossovers. Red vertical lines in the lowest panels show locations of the cross sections (XS1–XS4) in Fig. 3.

by the reversed secondary circulation, and stratification is restored before the flow enters the next bend. Similar interactions between stratification and secondary flows including the reversal of secondary circulation by the lateral baroclinic pressure gradient have been observed around a headland in the Hudson River estuary (Chant and Wilson 1997).

The lateral momentum balance (e.g., Chant and Wilson 1997; Nidzieko et al. 2009; Kranenburg et al. 2019) is examined to investigate the driving force for the secondary circulation patterns, with the depth-average lateral momentum balance

$$\frac{\partial u_r}{\partial t} = -\frac{u_s^2 - \overline{u_s^2}}{R} - \beta g \left(\int_z^0 \frac{\partial S}{\partial r} dz - \overline{\int_z^0 \frac{\partial S}{\partial r} dz} \right) - \left(u_s \frac{\partial u_r}{\partial s} - \overline{u_s \frac{\partial u_r}{\partial s}} \right) - \left(\frac{\partial \langle u_r' w' \rangle}{\partial z} - \frac{\tau_{b,r}}{\rho H} \right), \quad (1)$$

where Coriolis has been neglected. The u_s , u_r , and w terms are the streamwise, lateral, and vertical velocities; β is the

haline contraction coefficient; S is salinity; and $\tau_{b,r}$ is the lateral component of the bed shear stress. An overbar stands for depth average, and angle brackets represent a time average in the Reynolds stress. The time rate of change term is usually negligible due to the quasi-steady ebb flow. The first term on the right side is the centrifugal acceleration (CFA), and the second term is the baroclinic pressure gradient force (BCPG). The above forcing terms are typically balanced by the streamwise advective acceleration term (third term on the right side), i.e., the nonlocal adjustment of the secondary flow (e.g., Nidzieko et al. 2009), and the friction term (fourth term). Note that the depth-averaged momentum balance has been subtracted to investigate the vertical deviations of the driving forces, so that the barotropic pressure gradient does not appear in Eq. (1) (Nidzieko et al. 2009).

The CFA is inward in the lower layer and outward in the upper layer due to the vertical shear in the streamwise flow (Fig. 4d). This drives the “normal” secondary circulation

before the bend apex, which is identical to the sense of secondary circulation for homogeneous flow. The BCPG increases along the bend as a result of the lateral salinity gradient created by secondary circulation, and that opposes the CFA (Fig. 4e). Therefore, CFA + BCPG becomes outward in the lower layer and inward in the upper layer downstream of the bend apex (Fig. 4f), which thus reverses the sense of secondary circulation (Fig. 4c). As a result, the lateral circulation reverses sense and the associate lateral straining tends to be destratifying before the bend apex and restratifying after the bend apex (Fig. 4b). Moreover, a bottom salinity front can be observed along the inner bank upstream of the bend apex corresponding with the build up of high-salinity water there (Fig. 4a).

During flood tide (not shown), a more complex secondary circulation is observed in meanders. Streamwise velocity has lateral variations due to the channel curvature effect, and the lateral baroclinic pressure gradient forcing (BCPG) resulting from differential advection plays a more important role (e.g., Lacy and Monismith 2001; Nidzicko et al. 2009; Pein et al. 2018; Kranenburg et al. 2019). Multiple circulation cells appear in the bend during flood tide, leading to multiple regions of downwelling or upwelling (surface convergence or divergence) and resulting in both along-channel and lateral fluctuations in the salinity field. Note that the lateral BCPG during flood tide results from the differential advection of the along-estuary salinity gradient by the laterally sheared streamwise velocity, while the lateral BCPG during ebb tide is due to the interaction between stratification and the curvature-driven secondary circulation. Moreover, during flood tide, flow separation and recirculating eddies are observed in the lee of the bend apex, enhancing the lateral shear of the streamwise velocity and influencing the differential advection, lateral momentum balance, and secondary circulation.

Similar to ebb tide, during flood tide the meander regions have less stratification than in the straight channel case, but the following salinity variance budget analysis finds that more mixing occurs during ebb tides than flood tides (section 3c). During ebb tides, a single secondary circulation cell occurs and the longitudinal straining of the salinity gradient is stratifying. The stratification dynamics during flood have added complexity compared with the ebb, as advection of the along-channel salinity gradient leads to multiple secondary circulation cells and longitudinal straining tends to destratify the water column. Therefore, the subsequent analysis will examine in detail how channel curvature influences the stratification and mixing during ebb tides, and flood tide conditions will be addressed in section 5.

c. Vertical salinity variance budget

As illustrated in the channel cross sections in Fig. 3, the curvature-induced lateral circulation greatly affects the salinity distribution in the meanders. To quantify the variability in stratification and processes affecting it with channel curvature, we calculate the vertical salinity variance budget. The

depth-averaged vertical salinity variance budget is (Burchard and Rennau 2008; Li et al. 2018):

$$\frac{\partial}{\partial t} \frac{1}{h} \int (S'_v)^2 dz = -\frac{1}{h} \nabla \cdot \int \mathbf{u} (S'_v)^2 dz - \frac{1}{h} \int 2\mathbf{u}'_v S'_v \cdot \nabla \bar{S} dz - \frac{1}{h} \int 2K_z \left(\frac{\partial S}{\partial z} \right)^2 dz - \frac{1}{h} \int \mathcal{M}_{\text{num}} dz. \quad (2)$$

Parameter \bar{S} is the depth-averaged salinity, and S'_v is the deviation from the depth average; $(S'_v)^2$ is the vertical salinity variance that corresponds with stratification in the water column. The ∇ is the horizontal gradient operator, \mathbf{u} is the horizontal velocity vector (u_x and u_y), and \mathbf{u}'_v stands for vertical deviations. Parameter K_z is the vertical salinity mixing coefficient (eddy diffusivity). The vertical salinity variance budget is vertically integrated and averaged over the water depth h . The left side is the unsteady term (time rate of change). The first term on the right side is the advection term. The second term on the right side represents straining that can either increase or decrease the vertical variance, including both along-channel straining and lateral straining. The third term is physical mixing (dissipation of variance) that irreversibly decreases the vertical salinity variance. The fourth term is the additional numerical mixing due to discretization of tracer advection in the model (e.g., Burchard and Rennau 2008; Kalra et al. 2019).

The estuary-scale vertical salinity variance budget is evaluated over a control volume from 6 km (end of channel convergence) to 20 km (landward of salt intrusion). In the straight channel, stratification is created near the mouth during the ebb-to-flood transition by along-channel straining, because the tidal flow in the lower water column turns landward before the upper column due to baroclinicity. The stratification created near the mouth is advected into the control volume by flood currents as a positive term in the salinity variance budget (Fig. 5a). During flood tide in the straight channel, differential advection and baroclinic lateral circulation also tend to increase stratification with positive lateral straining (Lacy et al. 2003; Ralston and Stacey 2005a; Geyer et al. 2020). Stratification is decreased by the negative along-channel straining of boundary layer shear advecting saltier water over fresher water and by irreversible mixing. During ebb tide, stratification increases due to straining of the along-channel salinity gradient (Simpson et al. 1990), and diminishes after max ebb tide due to mixing. In contrast to flood tide, the lateral straining is almost negligible during the ebb. The unsteady term agrees well with summation of the other terms, indicating that the variance budget closes in the calculation. Numerical mixing is negligible in the straight channel through the entire tidal cycle.

In the sinuous model, the vertical salinity variance budget is overall similar to the straight channel model at the estuary scale (Fig. 5b), e.g., positive along-channel advection and negative along-channel straining during flood tide, and positive along-channel straining during ebb. However, numerical mixing accounts for around 30% of the total mixing in the sinuous model and the variance budget closes only when numerical

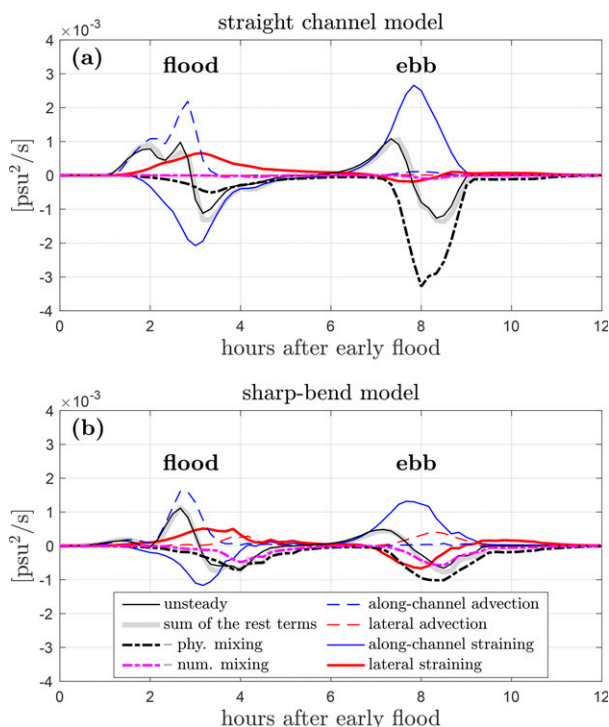


FIG. 5. Vertical salinity variance budget in the (a) straight channel model and (b) sharp-bend sinuous model, as a function of tidal hours. The budget is calculated as the spatial average over 6–20 km into the estuary. The solid black line is the unsteady term (time rate of change), and the solid gray line is the summation of the other terms that is supposed to balance with the unsteady term. See legend for details.

mixing is included. In addition, the net lateral straining is negative in the sinuous model during ebb, whereas in the straight channel the lateral straining during ebb was negligible. This suggests that curvature-induced lateral circulation plays a key role in the reduction in stratification, as will be examined below. The total lateral advection is expected to be zero because the control volume begins and ends in straight channel regions. However, positive values of total lateral advection appear in the sinuous model, due to the adjustment of the flow at transitions between meanders and straight channel regions, but the lateral advection term is always close to zero away from the transitions.

The laterally averaged vertical salinity variance budget is calculated to investigate the local effects of meanders during ebb (Fig. 6). The analysis primarily focuses on the second bend to avoid the initial flow adjustment from the straight channel in the first bend. Negative lateral straining before bend apices decreases vertical salinity variance and increases lateral variance, and lateral variance is converted back to vertical variance by the positive lateral straining after each bend apex (Figs. 6a,b). This alternating pattern of lateral straining is the same as the reduction in stratification by the normal secondary circulation upstream of the apex and the regeneration of stratification by the reversed secondary circulation downstream of the apex (section 3b). In straight channels, the

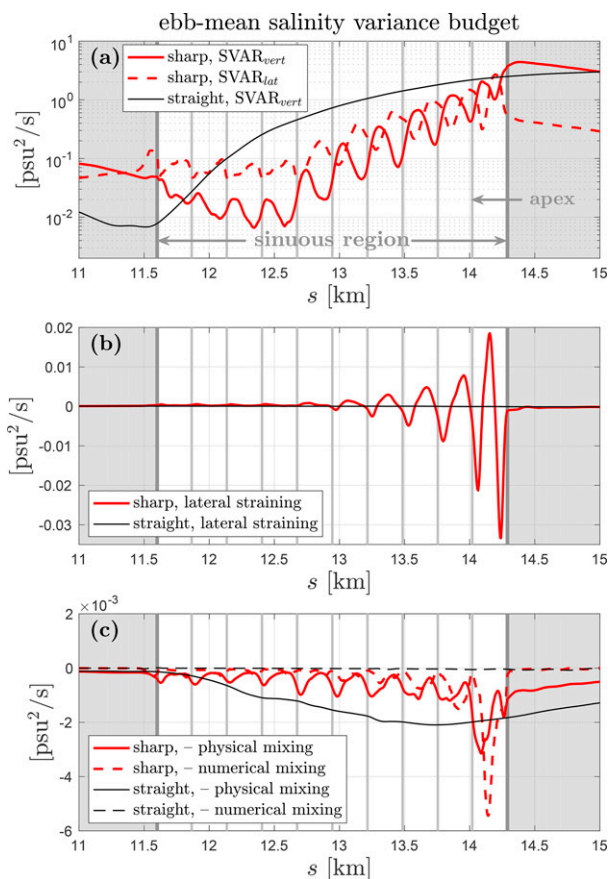


FIG. 6. Vertical salinity variance budget as a function of along-channel distance. The budget is laterally averaged, and calculated as the time average over ebb tide. (a) Vertical salinity variance (SVAR_{vert}) in the straight model and the sharp-bend sinuous model, and lateral salinity variance (SVAR_{lat}) in the sinuous channel. Note that the vertical axis is on a log scale in (a). See legend for details. (b) Lateral straining. (c) Physical mixing and numerical mixing. Note the different vertical axis ranges in (b) and (c). The vertical gray lines show the range of the sinuous region and locations of bend apices.

lateral straining typically increases stratification, e.g., due to the baroclinic two-cell lateral circulation during flood tides (Lerczak and Geyer 2004). However, negative lateral straining that decreases stratification occurs in the sinuous channel because of the additional forcing by the channel curvature.

While both positive and negative lateral straining occur in the sinuous channels, the integrated effect of the lateral straining during ebb is to decrease stratification. The lateral circulation and straining transfers salinity variance between vertical and lateral components through a bend. During the ebb tide, the magnitude of lateral straining decreases seaward through the meanders (Fig. 6b), because stratification overall decreases seaward and leads to less salinity variance for the lateral straining to convert back and forth in each consecutive bend (Fig. 6a). As a result, the reduction in stratification upstream of each bend apex by the negative straining is greater than the creation of stratification downstream of each

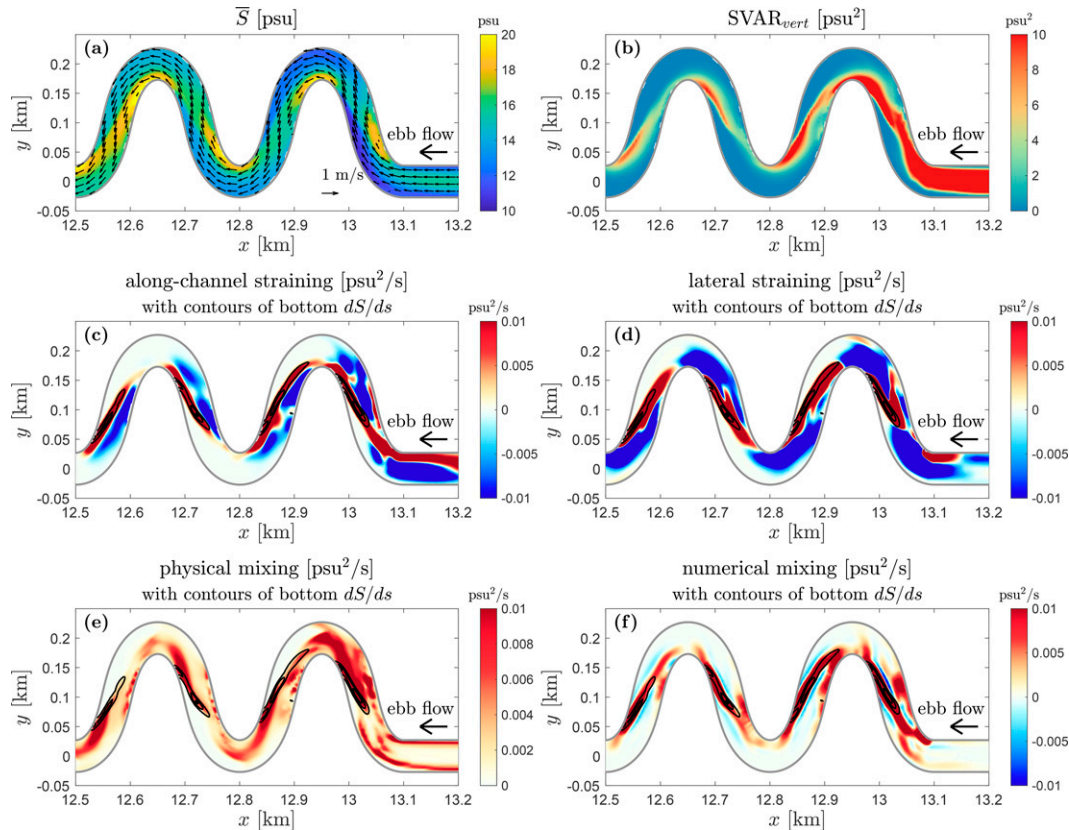


FIG. 7. Map views of the landward bends of the sharp-bend sinuous model at 2 h into ebb. (a) Depth-averaged salinity \bar{S} . (b) Vertical salinity variance $SVAR_{vert}$. (c) Along-channel straining, with contours of bottom along-channel salinity gradient. (d) Lateral straining. (e) Physical mixing. Positive values (red color) show magnitudes of physical mixing, but its influence is always to decrease the variance in the budget. (f) Numerical mixing. Note that negative numerical mixing can appear because of the antidiffusive corrections in the model (e.g., Burchard and Rennau 2008; Kalra et al. 2019), but the total numerical mixing is positive (dissipating the variance).

apex by positive straining. The net lateral straining is therefore negative (Fig. 5b), indicating an integrated effect to decrease stratification in meanders.

While straining can reduce stratification by converting it to horizontal salinity variance, mixing reduces stratification through the irreversible destruction of vertical salinity variance. Channel curvature can decrease stratification by locally enhancing vertical mixing (Fig. 6c). As the stratified flow enters the meanders, both physical mixing and numerical mixing are greater in the sinuous model than the straight model. Multiple hot spots of mixing are observed in meanders, mostly upstream of the bend apexes and close to the inner bank (Figs. 7e,f). Moreover, locations of enhanced mixing coincide with strong bottom along-channel salinity gradient, indicating that mixing in meanders is associated with bottom fronts (see details in section 4).

The strength of mixing decreases seaward as stratification is progressively destroyed by the mixing through the bends. Although strong mixing occurs in regions with channel curvature, the spatially integrated total mixing in the sinuous model is less than the straight model (Fig. 5). In the straight channel along-channel straining continuously creates stratification that

can then be mixed, whereas in the sinuous channel the enhanced mixing rapidly exceeds the along-channel straining, inhibiting the growth of stratification. Stratification progressively decreases through the bends due to this imbalance, reducing the stratification that could be mixed in bends downstream. Consequently, both the total mixing and the stratification in the sinuous channel are less than the straight channel.

Numerical mixing usually occurs at similar locations as physical mixing (Figs. 7e,f). While numerical mixing is greatest upstream of the bottom fronts in bends, physical mixing mostly occurs downstream of the fronts. Numerical mixing acts to diffuse horizontal gradients that otherwise would be smoothed by the turbulent or horizontal mixing processes, and the evolution of the stratification in the model is determined by the combination of physical mixing and numerical mixing (Ralston et al. 2017; Li et al. 2018). Numerical mixing is around 30% of the total mixing in the sharp-bend model, less than 20% in the smooth-bend model, and negligible in the straight channel model. While the different models have the same grid resolution and mixing schemes, the contribution of numerical mixing increases as channel curvature increases. Moreover, numerical mixing can be locally stronger than

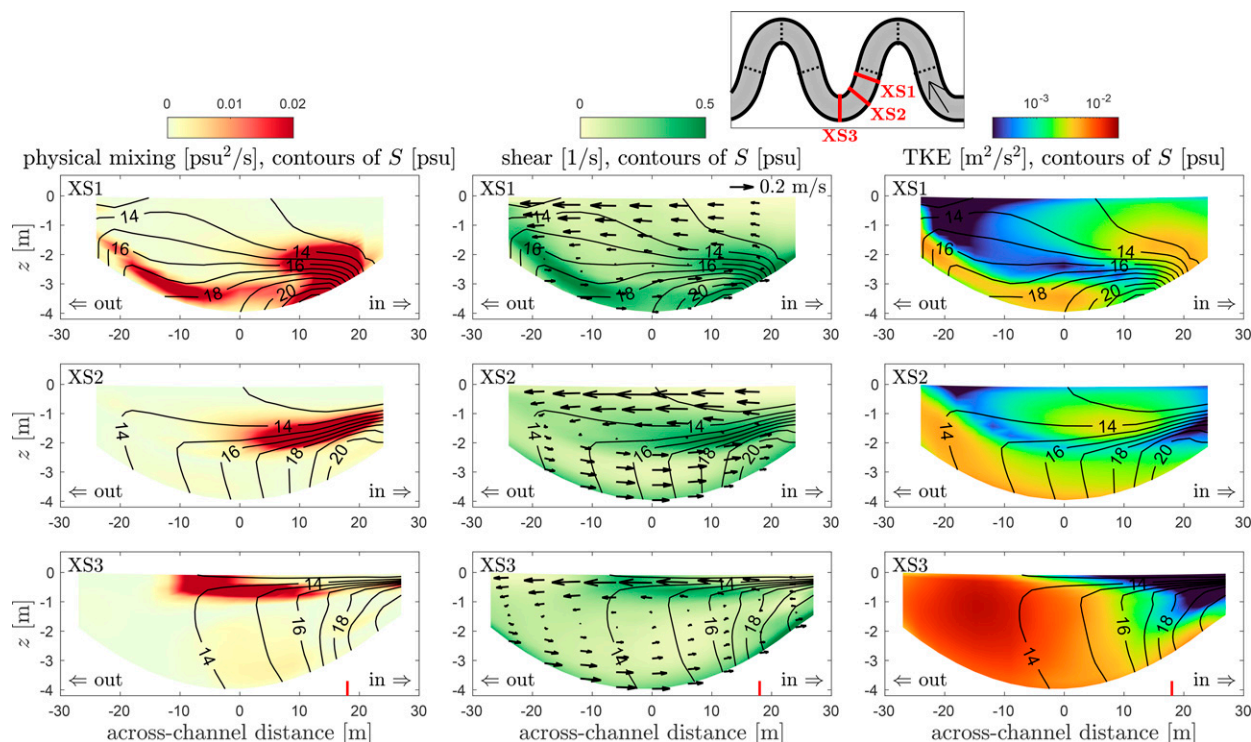


FIG. 8. (left) Physical mixing, (center) vertical shear, and (right) turbulent kinetic energy in three cross sections in a bend at 2 h into ebb tide. Salinity contours are shown in black. Arrows show the secondary circulation. The inner bank is on the right side, and outer bank is on the left side in all panels. In the small panel at the top, red lines show locations of the three cross sections, and dotted black lines represent the bend apexes and crossovers. The red vertical line in the lowest panels shows the location of the along-channel section (IB) in Fig. 9.

physical mixing, e.g., in the most landward bend (Fig. 6c). The results clearly demonstrate the importance of accurately representing numerical mixing in sinuous channels, and anywhere strong horizontal salinity gradients combined with streamwise currents (details examined in the analysis).

4. Analysis

a. Shear mixing at bend-scale salinity fronts

The salinity variance budget calculation suggested that channel curvature can decrease stratification through locally enhancing vertical mixing in meanders, with the strongest mixing occurring upstream of bend apexes (section 3c). In this section, we further investigate the three-dimensional distribution of mixing in a bend and the underlying mechanisms. Intense mixing happens near the inner bank as flow approaches the bend apex (Fig. 8, XS1–XS3) and the secondary circulation lifts the halocline upward (section 3b). The upstream edge of the intensified mixing corresponds with the bend-scale bottom salinity front near the inner bank (Fig. 9). Enhanced shear at the salinity front decreases the gradient Richardson number Ri_g to below the critical value, which allows for intensified turbulence and mixing (Figs. 9a,b).

Overturning mixing is found near the bend apex where secondary circulation tends to laterally advect saltier water over fresher water and create negative buoyancy (Fig. 8, XS3).

Maximum overturning mixing occurs near the bend apex (Fig. 10), in contrast to the shear-driven mixing that is strongest upstream of the apex. However, overturning mixing is minimal compared to the shear-driven mixing, with total overturning mixing that is $\sim 5\%$ of the shear mixing in the sharp-bend channel. For comparison, overturning was found to be the dominant source of mixing in a energetic tidal flow with channel curvature in Puget Sound by Seim and Gregg (1997) (e.g., their Fig. 15), whereas in the shallower tidal channel of Elkhorn Slough, Nidzieko et al. (2009) found that turbulent motions associated with the along-channel flow dominated the mixing rather than overturning. As found in the observations of overturning in Puget Sound (Seim and Gregg 1997), the strongest turbulent kinetic energy (TKE) in the sinuous model appears at the bend apex, and this turbulence could potentially drive mixing (Fig. 8, XS3). However, mixing requires both turbulence and stratification (Li et al. 2018; Warner et al. 2020). Stratification has been reduced by the negative lateral straining with channel curvature and thus mixing is relatively weak near bend apexes, even as the overturning circulation generates strong turbulence there. Note that ROMS is a hydrostatic model and nonhydrostatic processes associated with overturning may not be resolved, so the calculated contribution of overturning mixing should be considered approximate. Nevertheless, the estuarine dynamics are not favorable for overturning mixing in the sinuous channel because the sense of secondary circulation reverses

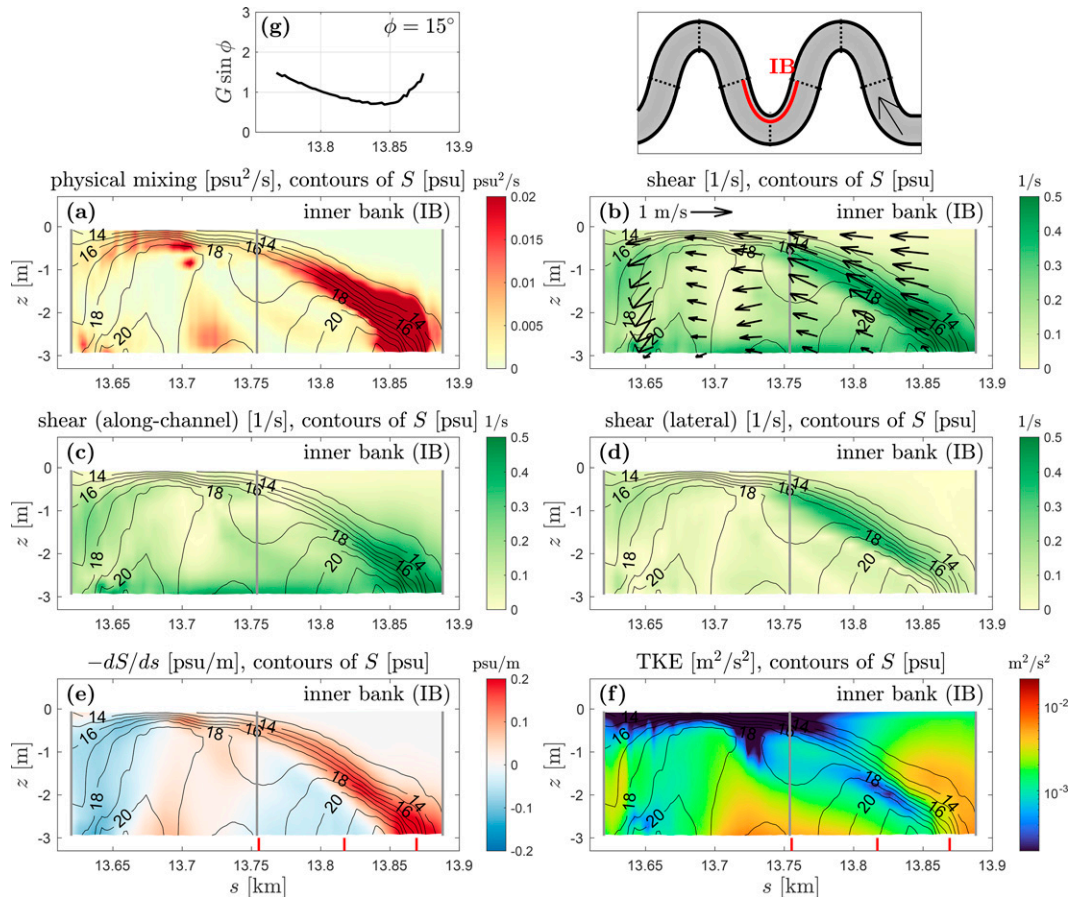


FIG. 9. An along-channel section near the inner bank of a bend (18 m from the centerline) at 2 h into ebb tide. (a) Physical mixing. Salinity contours are shown in black. The bend apex is marked by the gray line at around $s = 13.75$ km. (b)–(d) Total vertical shear, and the shear of along-channel flow and lateral flow. Black arrows show the streamwise and vertical velocities. (e) Along-channel salinity gradient. Red color means salinity increasing seaward. (f) Turbulent kinetic energy. (g) Composite Froude number G . The angle ϕ of the salinity front to the bottom velocity is around 15° (Froude angle). In the small map, the red line shows the along-channel section near the inner bank (IB). Dotted black lines represent the bend apex and crossovers. Red vertical lines in the lowest panels show locations of the cross sections (XS1–XS3) in Fig. 8.

downstream of the bend apex due to the lateral baroclinic pressure gradient (section 3b), effectively limiting the overturning to near the bend apex. This is in contrast to previous studies where overturning circulation could develop more continuously (Seim and Gregg 1997).

The most intense mixing is found upstream of bend apices, where bend-scale bottom salinity fronts provide a combination of stratification and active turbulence due to the strong vertical shear. Shear of the along-channel flow is amplified at bottom salinity fronts due to the combined influences of the bottom boundary layer (e.g., within 0.5–1 m above the bed) and baroclinicity. The along-channel baroclinic pressure gradient across the frontal zone can locally enhance the vertical shear of along-channel flow and thus lead to increased turbulence and mixing. Along-channel salinity gradients are tilted to the vertical direction by the enhanced shear, which corresponds with the positive along-channel straining observed near the toe of the bottom fronts (Fig. 7c) and adds to the

stratification available for mixing. As flow approaches the bend apex and the halocline rises to the upper column, the normal secondary circulation develops due to the channel curvature effect and, as a result, the shear of the lateral flow becomes greater than the along-channel component, contributing to the enhanced mixing (Fig. 7d).

Mixing is also locally enhanced near the outer bank at the entrance to the bend (e.g., Fig. 8, XS1), where the downward velocity of the secondary circulation pushes stratification into the bottom boundary layer. This is a second mechanism by which the curvature-induced lateral circulation brings together stratification and turbulence to increase mixing. The total mixing resulting from this vertical advection of stratification into the boundary layer is less than is associated with the bottom salinity front near the inner bank.

While we have focused on physical mixing in this analysis, the numerical mixing has similar spatial and temporal distribution patterns as the physical mixing, so it does not alter the

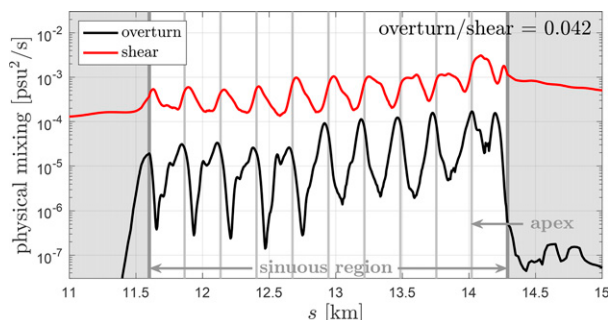


FIG. 10. Laterally averaged shear mixing and overturning mixing as a function of along-channel distance, averaged over ebb tide. Note the vertical axis has a log scale. The vertical gray lines show the range of the sinuous region and locations of bend apexes.

underlying mechanisms. Numerical mixing arises from the advection of salinity gradients, and the regions of physical mixing typically have sharp salinity gradients and strong velocities that can thus lead to numerical mixing. In an along-channel section near the inner bank, strong numerical mixing occurs at the bend-scale salinity front (not shown) in a similar form as physical mixing (Fig. 9a), except that numerical mixing happens slightly upstream of the frontal zone (also reflected in Figs. 7e,f).

b. Frontogenesis in meanders

To characterize the bottom fronts that cause mixing in the sinuous model, frontogenesis in meanders is analyzed by using the tendency equation of along-channel salinity gradient (Geyer and Ralston 2015)

$$\begin{aligned} \frac{\partial}{\partial t} \frac{\partial S}{\partial s} + \mathbf{u} \cdot \nabla \frac{\partial S}{\partial s} = & -\frac{\partial u_s}{\partial s} \frac{\partial S}{\partial s} - \frac{\partial u_r}{\partial s} \frac{\partial S}{\partial r} - \frac{\partial w}{\partial s} \frac{\partial S}{\partial z} \\ & - \frac{\partial}{\partial s} \frac{\partial}{\partial z} \langle S'w' \rangle. \end{aligned} \quad (3)$$

The left-side terms represent the local tendency and advection of the along-channel salinity gradient. Terms on the right side represent physical processes that affect the along-channel salinity gradient, including the along-channel convergence/divergence (first term), twisting of lateral and vertical salinity gradients due to the along-channel gradients in lateral and vertical velocity (second and third term, respectively). The fourth term on the right side is the along-channel gradient of vertical mixing, which is negligible here because the idealized channels have uniform cross-sectional shape and do not have steeply sloping bathymetry that might create spatial gradients in mixing in the along-channel direction.

In straight channels, generation of along-estuary bottom salinity fronts is typically dominated by the along-channel convergence (first term on the right side) (e.g., Geyer and Ralston 2015). However, in sinuous estuarine channels, the secondary circulation can make lateral and vertical processes more important for frontogenesis. Near the toe of the bottom front, formation of the along-channel salinity gradient is dominated by the lateral process (second term) (Fig. 11b). The

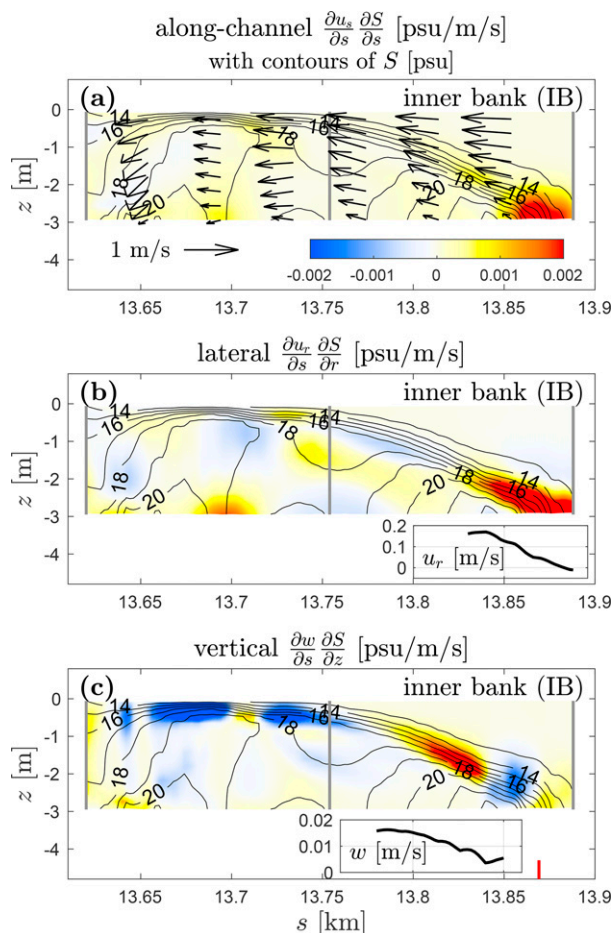


FIG. 11. Terms affecting the along-channel salinity gradient in Eq. (3). (a) Along-channel convergence. Salinity contours are shown in black. Black arrows show the streamwise and vertical velocities. (b) Twisting of lateral salinity gradients due to the along-channel gradient in lateral velocity. The small panel shows the along-channel distribution of near-bed lateral velocity (positive means toward the inner bend). (c) Twisting of vertical salinity gradients due to the along-channel gradient in vertical velocity. The small panel shows the along-channel change of vertical velocity in the midwater column. Red color means contributing to the generation of the along-channel front. This is the same along-channel section near the inner bank (IB) as in Fig. 9, at 2 h into ebb tide. The red vertical line in the lowest panels marks the location of the cross section (XS1) near the toe of the front.

inward secondary flow near the bed develops after flow enters the bend, twisting lateral salinity gradients into the along-channel direction. In the midwater column, the upward vertical velocity near the inner bank increases as stratified flow goes toward the bend apex, and vertical salinity gradients are thus distorted into the along-channel direction (third term), contributing to formation of the along-channel salinity front (Fig. 11c).

The twisting of lateral salinity gradients by lateral currents is the biggest contributor to frontogenesis, and the source of the lateral salinity gradient has been investigated by the

tendency equation of lateral salinity gradient [not shown, similar to Eq. (3)]. Generation of the lateral salinity gradient is mainly driven by the lateral gradient of vertical mixing in the parabolic cross section, where the shallow bathymetry at the channel edges creates stronger vertical mixing, similar to the horizontal salinity gradient formed over the shelf slope (e.g., Gawarkiewicz and Chapman 1992; Lerczak and Geyer 2004; McWilliams 2021). As a result, strong lateral salinity gradients occur in the inner bend near the toe of the bottom front with lower salinity near the bank (e.g., Fig. 3, XS1), which then is twisted by the secondary flow and leads to generation of the along-channel front (Fig. 11b).

Overall, the frontogenesis analysis suggests that both the curvature-induced secondary circulation, i.e., the lateral and vertical flows, and the lateral variability of bathymetry and associated boundary layer mixing are crucial for the formation of along-channel salinity fronts in meanders. The bottom salinity fronts that result from the curvature-induced secondary circulation provide the dominant mechanism for mixing and explain the decreased stratification in the sinuous channel.

To understand the hydraulic state of the curvature-induced bottom front, we calculate the composite Froude number G for two-layer flow (e.g., Armi and Farmer 1986; Geyer and Ralston 2015):

$$G^2 = F_1^2 + F_2^2 = \frac{u_1^2}{g'H_1} + \frac{u_2^2}{g'H_2}, \quad (4)$$

where F_1 and F_2 are the Froude numbers for the upper and lower layers, u_1 and u_2 are the average velocities of each layer, and H_1 and H_2 are the layer thickness. The term $g' = g(\Delta\rho/\bar{\rho})$ is the reduced gravity based on the density difference between the upper and lower layers. The bottom front is obliquely oriented to the channel flow, and the angle ϕ of the front to the bottom velocity is around 15° (Fig. 7). The effective composite Froude number $G\sin\phi$ is calculated to account for the Froude angle theory in MacDonald and Geyer (2005), i.e., evaluate the component of G normal to the front. The bottom front in the bend exists during around 1–3 h into ebb and is relatively stationary. The $G\sin\phi$ is close to 1 (critical condition) at the toe of the bottom front (Fig. 9g), and thus, the stationary and oblique bottom front is consistent with a critical front (MacDonald and Geyer 2005).

c. Simpson number in sinuous estuarine channels

Stratification is decreased in the sinuous channel cases due to enhanced vertical mixing, and we would like to relate that to implications for stratification in the broader estuarine parameter space. One approach is to consider the Simpson number Si , which is defined as the ratio of potential energy input due to tidal straining to tidal mixing (Stacey et al. 2001; Burchard et al. 2011; Geyer and Ralston 2011)

$$Si = \frac{\beta g(\partial S/\partial s)H^2}{C_D u_T^2}. \quad (5)$$

Parameter $\partial S/\partial s$ is the along-estuary salinity gradient (typically taken over the estuary scale), C_D is the drag coefficient,

and u_T is the tidal velocity. The Si relates to stratification conditions in estuaries because it represents the balance between the creation of stratification by along-estuary straining and destruction of stratification due to vertical mixing (Stacey et al. 2001).

The drag coefficient C_D in the denominator of Si relates to the strength of tidal mixing. The C_D is a typical way to quantify the drag force experienced by the tidal flow, and C_D also relates to the turbulent energy dissipation rate and the strength of turbulent mixing. Drag in estuarine channels is usually attributed to bottom friction, and a common value for C_D is around 0.003 (e.g., Dronkers 1964; Sternberg 1968; Soulsby 1990). However, channel curvature can lead to an increased C_D of up to ~ 5 times larger than the typical value by enhancing bottom shear stress and creating form drag (e.g., Chang 1984; Warner and MacCready 2014; Bo and Ralston 2020).

The present study indicates that channel curvature can lead to decreased stratification through enhanced vertical mixing (sections 3a and 4a), and this is consistent with the increased drag and turbulent dissipation found in sinuous channels from previous studies. To link the tidal energy dissipation to the strengthened mixing and decreased stratification, we can use the increased value of C_D for the sinuous channel in the Si calculation. The C_D is evaluated in the model results based on the momentum equation over a length scale similar to the meander length (Bo and Ralston 2020), and this calculated C_D represents the total drag on the flow including, e.g., enhanced bottom shear stress caused by secondary circulation and form drag due to flow separation across the bend. While C_D ranges between 0.002 and 0.004 in the straight channel models depending on stratification conditions, C_D is increased to 0.005–0.007 in the smooth bend models and 0.009–0.010 in the sharp bend models due to the channel curvature effect.

The strength of the stratification is quantified using the buoyancy frequency N (e.g., Stacey et al. 2011), which is defined by

$$N^2 = -\frac{g}{\rho} \frac{\partial \rho}{\partial z} \approx -\frac{\beta g \Delta S}{H}, \quad (6)$$

where ΔS is the bottom-surface salinity difference. The Si and N^2 are calculated for the straight and sinuous models (Table 1; Fig. 12). Only ebb tide results are analyzed because we have focused on the flow patterns and mixing mechanisms of ebb tides, and the stratifying along-estuary straining represented in Si only occurs during ebb tides. The $\partial S/\partial s$ is estimated using the maximum along-channel gradient during ebb near the meander region, which typically appears when the salinity intrusion retreats to the meander region. The H is the channel thalweg depth, u_T is the tidal maximum, and C_D is calculated around the maximum tidal velocity. In this way, the estimated Si characterizes the ratio of maximum straining and maximum mixing during the ebb tide.

The calculated C_D is generally 0.005–0.01 in the sinuous channel models, up to 3 times greater than the typical value 0.003 but comparable to the observed C_D of 0.005–0.02 in the North River estuary (Bo et al. 2021). In the deeper straight

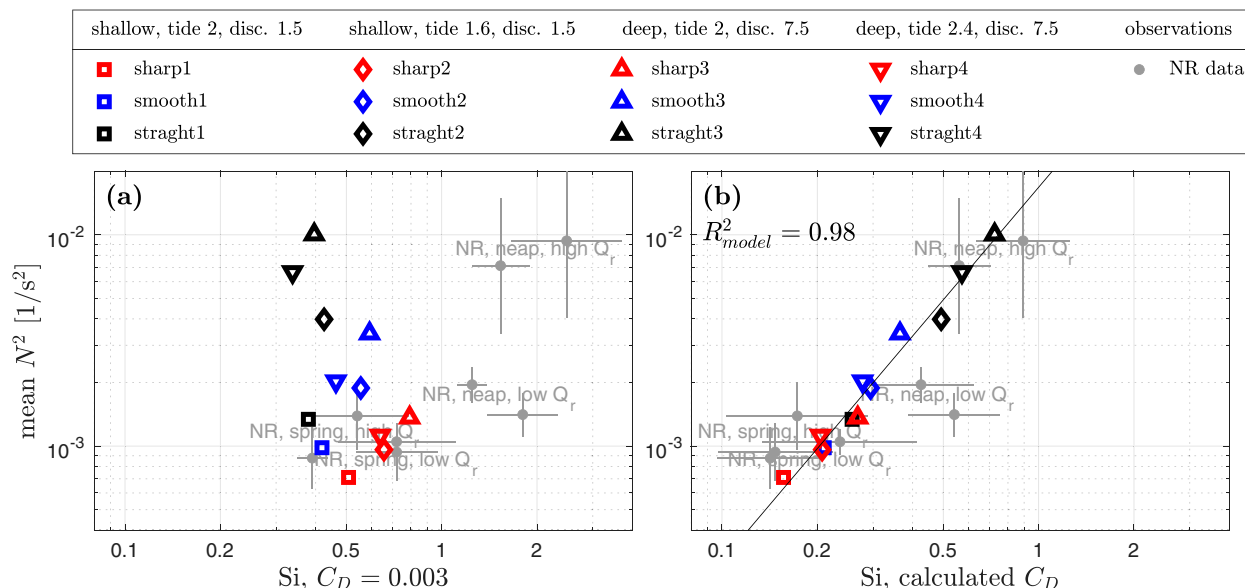


FIG. 12. N^2 vs Si . Si is defined based on (a) a constant $C_D = 0.003$ and (b) the calculated C_D from the momentum budget. See legends for the channel shape and tidal and discharge conditions of the 12 idealized models (Table 1), and the black line in (b) shows the linear regression for the model results. Gray dots are the observational data from the North River (NR) estuary with spring/neap tides and high/low discharge (Q_r) conditions. The N^2 (s^{-2}) generally scales with ΔS (psu) divided by 100.

channel models with strong stratification, C_D is 0.0015–0.002 and smaller than the typical value 0.003 because turbulence has been inhibited by stratification. Defining Si based on a constant $C_D = 0.003$ leads to a scattered N^2 – Si plot and no dependence of stratification on Si in the model results (Fig. 12a). Typically a Si close to 1 corresponds with stratified conditions during the ebb tide (e.g., Geyer and MacCready 2014; Geyer et al. 2020). However, using $C_D = 0.003$ for the sharp-bend models results in Si of around 1 for periods with weak ebb stratification of N^2 of 0.001 (corresponding to $\Delta S \sim 1$) (Fig. 12a). This suggests that defining Si based on $C_D = 0.003$ underestimates the turbulent energy dissipation rate and strength of mixing in sinuous channels. Alternatively, for the deeper straight channel models that are strongly stratified during ebbs, using a constant $C_D = 0.003$ leads to an overestimate of mixing and an underestimate of Si (Fig. 12a). By contrast, N^2 has a positive dependence on Si that incorporates the calculated C_D , and the simulation results collapse onto a single line (Fig. 12b). The strong correlation between N^2 and Si emphasizes the importance of using an appropriate C_D in calculating Si .

For comparison, we have plotted observational data from the North River estuary collected in 2017 from April to July (Kranenburg et al. 2019; Bo et al. 2021). The tidal range varied with the spring–neap cycle between 2 and 3 m, and the river discharge was 1–10 $m^3 s^{-1}$ during the observational period. Stratification in the North River estuary varied tidally and with tidal and discharge conditions, with ΔS between 0 and 20 psu. The observations covered a representative range of spring/neap tides and high/low discharge periods. Average values of N^2 and Si and the standard deviations of two 3-day

windows (six tidal cycles) are shown for spring/neap tides and for high/low discharge conditions (Fig. 12). The North River N^2 and Si are calculated for the midestuary region that includes several bends with the curvature ratio R/W ranging between 1 and 2 and has a typical channel depth of 5 m. The channel geometry and estuarine conditions of the idealized models are broadly similar to the observed range of the North River estuary.

Defining Si based on $C_D = 0.003$ for the North River observations leads to Si of around 1 during high/low discharge spring tide conditions and low discharge neap tide conditions that were weakly stratified (Fig. 12a), whereas strong stratification would typically be expected for Si values of around 1 (Geyer and MacCready 2014; Geyer et al. 2020). Incorporating the increased C_D into Si for the North River observations leads to values of Si that make the observed stratification more consistent with results from other systems (Fig. 12b). Note that the correlation between N^2 and Si is similar for the observations with $C_D = 0.003$ or the calculated C_D , because the calculated C_D in the North River estuary has less variability than the idealized models with different channel morphology, and the key difference in the observational results is the general shift in Si values. Overall, our analysis suggests that incorporating a representative C_D into the Si scaling can be an effective way to predict stratification conditions in estuarine channels with curvature.

5. Discussion

The present research finds that bend-scale bottom fronts can be generated in meanders during ebb tides (Fig. 13). The bottom fronts result from the combined effects of curvature-

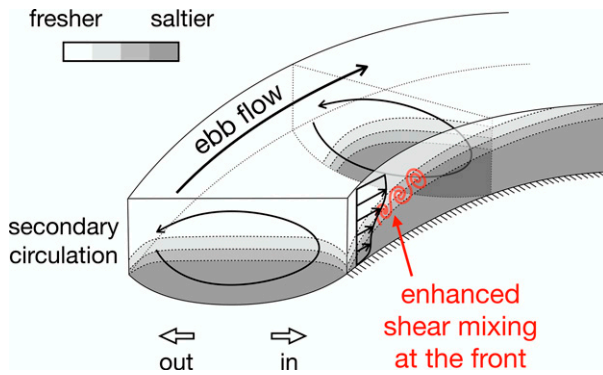


FIG. 13. A schematic plot of flow, salinity, and frontogenesis in an estuarine bend. The stratified ebb flow goes into the bend, with secondary circulation in the cross sections. The gray colors and dashed lines represent salinity and isohalines. An along-channel front is created in the inner bend due to the interaction between secondary circulation and the stratified flow. Enhanced shear mixing occurs at the front.

induced secondary circulation, stratification, and boundary layer mixing (twisting of lateral and vertical gradients into the along-channel direction, section 4b). The vertical shear of along-channel velocity is enhanced at these salinity fronts due to the along-channel baroclinic pressure gradient across the front (e.g., Geyer and Ralston 2015; Warner et al. 2020). As a result, enhanced shear mixing occurs at bend-scale salinity fronts, providing the dominant source of mixing that leads to weaker stratification in meanders.

The analysis has focused on the shallower sharp-bend model with 2-m range tides and $1.5 \text{ m}^3 \text{ s}^{-1}$ discharge, but similar curvature-induced bottom fronts and shear mixing also appear in all the other sinuous channel cases with sharp or smooth bends, shallower (4 m) or deeper (6 m) thalweg depth, and different tidal and discharge conditions. While the bend-scale bottom fronts are commonly found in these idealized sinuous estuaries, corroborating observational evidence is needed. Lateral bathymetric variability that leads to lateral variations in boundary layer mixing is important for frontogenesis, and therefore, local bathymetric features in bends that are not present in the idealized channels, e.g., points bars, scour holes, sills, and shallow shoals, may introduce additional complexity to the frontogenesis.

The present research has focused on relatively shallow tidal channels, e.g., less than 10 m, but similar mixing fronts are also expected to occur in other estuarine and coastal environments with flow curvature, e.g., deeper estuaries and around headlands. The spinup time of secondary circulation relates to the lateral advection time scale

$$T_{\text{adv,lat}} = \frac{W}{u_r}, \tag{7}$$

which is around 10 min for the model tidal channels with width W around 50 m and lateral velocity u_r around 0.1 m s^{-1} .

The time scale for bottom boundary layer mixing and generation of bottom fronts can be described by the frictional time scale (Geyer 1993a; Chant and Wilson 1997)

$$T_f = \frac{H}{C_f u_s}, \tag{8}$$

where C_f is the bottom friction coefficient, similar to C_D except that it only accounts for the bottom shear stress but not the total drag. We estimate that T_f is around 40 min using $H = 4 \text{ m}$, $C_f = 0.003$, and $u_s = 0.5 \text{ m s}^{-1}$. Both $T_{\text{adv,lat}}$ and T_f are much less than the 12-h tidal time scale, which allows for frontogenesis and the associated mixing to occur in shallow tidal channels. However, in deeper channels, taking the Tacoma Narrows of Puget Sound in Seim and Gregg (1997) as an example, $T_{\text{adv,lat}} \approx 2 \text{ h}$ with $W = 1500 \text{ m}$ and $u_r = 0.2 \text{ m s}^{-1}$, and $T_f \approx 18 \text{ h}$ with $H = 100 \text{ m}$, $C_f = 0.003$, and $u_s = 0.5 \text{ m s}^{-1}$. The T_f can be larger than the tidal time scale for deep systems, potentially limiting the growth of bottom fronts and strength of shear mixing. Therefore, overturning mixing may play a more important role as in Seim and Gregg (1997). As a comparison, the ratio of overturning mixing to shear mixing increases by a factor of 1.5 in our deeper sharp-bend model compared to the shallower sharp-bend model, though it remains small overall. Internal wave generation and breaking from flow around topographic features may also contribute to mixing in deep estuarine channels, as was observed in curved tidal flows around headlands by Edwards et al. (2004).

The mixing and frontogenesis have been investigated for ebb tides, when the alternating normal and reversed lateral circulations occur in meanders. Bend-scale bottom fronts are also expected to be found during flood tides that have similar lateral circulation patterns (e.g., Seim and Gregg 1997; Chant and Wilson 1997). However, more complex secondary circulation can develop during flood tides as a result of differential advection due to the channel curvature effect (Lacy and Monismith 2001; Nidzicko et al. 2009; Pein et al. 2018; Kranenburg et al. 2019). Multiple circulation layers in the vertical and multiple cells in the lateral can occur, leading to salinity fronts with more complex structures. The locations and mechanisms of enhanced mixing during flood tides, as well as frontogenesis associated with twisting by lateral and vertical flows, thus require more detailed investigation.

Moreover, flow separation can occur during flood tide behind the bend apex with eddies generated in the inner bend and main flow separated toward the outer bend (Bo and Ralston 2020). The strong lateral shear across the boundary of the separation zone can further enhance the differential advection, and thus potentially affects secondary circulation, frontogenesis, and mixing. The increased C_D in the Si scaling (section 4c) can include both bottom friction enhancement associated with secondary circulation and form drag due to flow separation (e.g., Chang 1984; Bo et al. 2021), but the respective influences of enhanced bottom stress and form drag on mixing are not clear. The linkage between drag increase and mixing enhancement, especially for form drag, still merits further investigation.

6. Conclusions

Stratification is decreased in the idealized sinuous estuaries compared to straight channel estuaries. Analysis of the vertical salinity variance budget reveals that channel curvature can affect stratification through generation of alternating signs of lateral straining and through local intensification of mixing. The mixing in meanders is dominated by shear mixing at bend-scale bottom fronts rather than overturning mixing. These bottom fronts are generated as a product of interaction between the secondary circulation and stratification, and also depend on lateral bathymetric variations. Finally, an adjusted Simpson number that incorporates the increased drag coefficient with channel curvature can be used to parameterize the decreased stratification and enhanced vertical mixing associated with meanders.

Acknowledgments. The research leading to these results was funded by NSF Awards OCE-1634481 and OCE-2123002. The authors thank W. R. Geyer and A. M. P. Garcia for helpful discussions. Suggestions and comments provided by two anonymous reviewers are greatly appreciated.

Data availability statement. Model data supporting this study are available online: <https://doi.org/10.5281/zenodo.5722603>; <https://doi.org/10.5281/zenodo.5725012>; <https://doi.org/10.5281/zenodo.5725153>; <https://doi.org/10.5281/zenodo.5725189>.

REFERENCES

- Apmann, R. P., 1964: A case history in theory and experiment: Fluid flow in bends. *Isis*, **55**, 427–434, <https://doi.org/10.1086/349899>.
- Armi, L., and D. Farmer, 1986: Maximal two-layer exchange through a contraction with barotropic net flow. *J. Fluid Mech.*, **164**, 27–51, <https://doi.org/10.1017/S0022112086002458>.
- Becherer, J., M. T. Stacey, L. Umlauf, and H. Burchard, 2015: Lateral circulation generates flood tide stratification and estuarine exchange flow in a curved tidal inlet. *J. Phys. Oceanogr.*, **45**, 638–656, <https://doi.org/10.1175/JPO-D-14-0001.1>.
- Bo, T., and D. K. Ralston, 2020: Flow separation and increased drag coefficient in estuarine channels with curvature. *J. Geophys. Res. Oceans*, **125**, e2020JC016267, <https://doi.org/10.1029/2020JC016267>.
- , —, W. M. Kranenburg, W. R. Geyer, and P. Traykovski, 2021: High and variable drag in a sinuous estuary with intermittent stratification. *J. Geophys. Res. Oceans*, **126**, e2021JC017327, <https://doi.org/10.1029/2021JC017327>.
- Burchard, H., and H. Rennau, 2008: Comparative quantification of physically and numerically induced mixing in ocean models. *Ocean Modell.*, **20**, 293–311, <https://doi.org/10.1016/j.oceanmod.2007.10.003>.
- , R. D. Hetland, E. Schulz, and H. M. Schuttelaars, 2011: Drivers of residual estuarine circulation in tidally energetic estuaries: Straight and irrotational channels with parabolic cross section. *J. Phys. Oceanogr.*, **41**, 548–570, <https://doi.org/10.1175/2010JPO4453.1>.
- Chang, H. H., 1984: Variation of flow resistance through curved channels. *J. Hydraul. Eng.*, **110**, 1772–1782, [https://doi.org/10.1061/\(ASCE\)0733-9429\(1984\)110:12\(1772\)](https://doi.org/10.1061/(ASCE)0733-9429(1984)110:12(1772)).
- Chant, R. J., and R. E. Wilson, 1997: Secondary circulation in a highly stratified estuary. *J. Geophys. Res.*, **102**, 23 207–23 215, <https://doi.org/10.1029/97JC00685>.
- Dronkers, J. J., 1964: *Tidal Computations in Rivers and Coastal Waters*. North-Holland Publishing Company, 518 pp.
- Edwards, K. A., P. MacCready, J. N. Moum, G. Pawlak, J. M. Klymak, and A. Perlin, 2004: Form drag and mixing due to tidal flow past a sharp point. *J. Phys. Oceanogr.*, **34**, 1297–1312, [https://doi.org/10.1175/1520-0485\(2004\)034<1297:FDAMDT>2.0.CO;2](https://doi.org/10.1175/1520-0485(2004)034<1297:FDAMDT>2.0.CO;2).
- Fagherazzi, S., E. J. Gabet, and D. J. Furbish, 2004: The effect of bidirectional flow on tidal channel planforms. *Earth Surf. Processes Landforms*, **29**, 295–309, <https://doi.org/10.1002/esp.1016>.
- Farmer, D. M., and J. D. Smith, 1980: Tidal interaction of stratified flow with a sill in knight inlet. *Deep-Sea Res.*, **27A**, 239–254, [https://doi.org/10.1016/0198-0149\(80\)90015-1](https://doi.org/10.1016/0198-0149(80)90015-1).
- Garcia, A. M. P., W. R. Geyer, and N. Randall, 2021: Exchange flows in tributary creeks enhance dispersion by tidal trapping. *Estuaries Coasts*, **45**, 363–381, <https://doi.org/10.1007/s12237-021-00969-4>.
- Garvine, R. W., 1974: Dynamics of small-scale oceanic fronts. *J. Phys. Oceanogr.*, **4**, 557–569, [https://doi.org/10.1175/1520-0485\(1974\)004<0557:DOSSOF>2.0.CO;2](https://doi.org/10.1175/1520-0485(1974)004<0557:DOSSOF>2.0.CO;2).
- Gawarkiewicz, G., and D. C. Chapman, 1992: The role of stratification in the formation and maintenance of shelf-break fronts. *J. Phys. Oceanogr.*, **22**, 753–772, [https://doi.org/10.1175/1520-0485\(1992\)022<0753:TROSIT>2.0.CO;2](https://doi.org/10.1175/1520-0485(1992)022<0753:TROSIT>2.0.CO;2).
- Geyer, W. R., 1993a: The importance of suppression of turbulence by stratification on the estuarine turbidity maximum. *Estuaries*, **16**, 113–125, <https://doi.org/10.2307/1352769>.
- , 1993b: Three-dimensional tidal flow around headlands. *J. Geophys. Res.*, **98**, 955–966, <https://doi.org/10.1029/92JC02270>.
- , and D. K. Ralston, 2011: The dynamics of strongly stratified estuaries. *Treatise on Estuarine and Coastal Science*, E. Wolanski and D. McLusky, Eds., Academic Press, 37–51.
- , and P. MacCready, 2014: The estuarine circulation. *Annu. Rev. Fluid Mech.*, **46**, 175–197, <https://doi.org/10.1146/annurev-fluid-010313-141302>.
- , and D. K. Ralston, 2015: Estuarine frontogenesis. *J. Phys. Oceanogr.*, **45**, 546–561, <https://doi.org/10.1175/JPO-D-14-0082.1>.
- , —, and R. C. Holleman, 2017: Hydraulics and mixing in a laterally divergent channel of a highly stratified estuary. *J. Geophys. Res. Oceans*, **122**, 4743–4760, <https://doi.org/10.1002/2016JC012455>.
- , —, and J.-L. Chen, 2020: Mechanisms of exchange flow in an estuary with a narrow, deep channel and wide, shallow shoals. *J. Geophys. Res. Oceans*, **125**, e2020JC016092, <https://doi.org/10.1029/2020JC016092>.
- Grant, W. D., and O. S. Madsen, 1982: Movable bed roughness in unsteady oscillatory flow. *J. Geophys. Res.*, **87**, 469–481, <https://doi.org/10.1029/JC087iC01p00469>.
- Haidvogel, D. B., and Coauthors, 2008: Ocean forecasting in terrain-following coordinates: Formulation and skill assessment of the regional ocean modeling system. *J. Comput. Phys.*, **227**, 3595–3624, <https://doi.org/10.1016/j.jcp.2007.06.016>.
- James, C., 1994: Evaluation of methods for predicting bend loss in meandering channels. *J. Hydraul. Eng.*, **120**, 245–253, [https://doi.org/10.1061/\(ASCE\)0733-9429\(1994\)120:2\(245\)](https://doi.org/10.1061/(ASCE)0733-9429(1994)120:2(245)).
- Kalra, T. S., X. Li, J. C. Warner, W. R. Geyer, and H. Wu, 2019: Comparison of physical to numerical mixing with different tracer advection schemes in estuarine environments. *J. Mar. Sci. Eng.*, **7**, 338, <https://doi.org/10.3390/jmse7100338>.

- Kranenburg, W. M., W. R. Geyer, A. M. P. Garcia, and D. K. Ralston, 2019: Reversed lateral circulation in a sharp estuarine bend with weak stratification. *J. Phys. Oceanogr.*, **49**, 1619–1637, <https://doi.org/10.1175/JPO-D-18-0175.1>.
- Lacy, J. R., and S. G. Monismith, 2001: Secondary currents in a curved, stratified, estuarine channel. *J. Geophys. Res.*, **106**, 31 283–31 302, <https://doi.org/10.1029/2000JC000606>.
- , M. T. Stacey, J. R. Burau, and S. G. Monismith, 2003: Interaction of lateral baroclinic forcing and turbulence in an estuary. *J. Geophys. Res.*, **108**, 3089, <https://doi.org/10.1029/2002JC001392>.
- Langbein, W. B., 1963: The hydraulic geometry of a shallow estuary. *Hydrol. Sci. J.*, **8**, 84–94, <https://doi.org/10.1080/02626666309493340>.
- , and L. B. Leopold, 1970: River meanders and the theory of minimum variance. *Rivers and River Terraces*, Springer, 238–263.
- Leeder, M. R., and P. H. Bridges, 1975: Flow separation in meander bends. *Nature*, **253**, 338–339, <https://doi.org/10.1038/253338a0>.
- Leopold, L. B., 1960: *Flow Resistance in Sinuous or Irregular Channels*. US Government Printing Office, 24 pp.
- , and M. G. Wolman, 1960: River meanders. *Geol. Soc. Amer. Bull.*, **71**, 769–793, [https://doi.org/10.1130/0016-7606\(1960\)71\[769:RM\]2.0.CO;2](https://doi.org/10.1130/0016-7606(1960)71[769:RM]2.0.CO;2).
- Lerczak, J. A., and W. R. Geyer, 2004: Modeling the lateral circulation in straight, stratified estuaries. *J. Phys. Oceanogr.*, **34**, 1410–1428, [https://doi.org/10.1175/1520-0485\(2004\)034<1410:MTLCIS>2.0.CO;2](https://doi.org/10.1175/1520-0485(2004)034<1410:MTLCIS>2.0.CO;2).
- Li, X., W. R. Geyer, J. Zhu, and H. Wu, 2018: The transformation of salinity variance: A new approach to quantifying the influence of straining and mixing on estuarine stratification. *J. Phys. Oceanogr.*, **48**, 607–623, <https://doi.org/10.1175/JPO-D-17-0189.1>.
- MacDonald, D. G., and W. R. Geyer, 2005: Hydraulic control of a highly stratified estuarine front. *J. Phys. Oceanogr.*, **35**, 374–387, <https://doi.org/10.1175/JPO-2692.1>.
- Marani, M., S. Lanzoni, D. Zandolin, G. Seminara, and A. Rinaldo, 2002: Tidal meanders. *Water Resour. Res.*, **38**, 1225, <https://doi.org/10.1029/2001WR000404>.
- McWilliams, J. C., 2021: Oceanic frontogenesis. *Annu. Rev. Mar. Sci.*, **13**, 227–253, <https://doi.org/10.1146/annurev-marine-032320-120725>.
- Nidzicko, N. J., J. L. Hench, and S. G. Monismith, 2009: Lateral circulation in well-mixed and stratified estuarine flows with curvature. *J. Phys. Oceanogr.*, **39**, 831–851, <https://doi.org/10.1175/2008JPO4017.1>.
- Nunes, R., and J. Simpson, 1985: Axial convergence in a well-mixed estuary. *Estuarine Coastal Shelf Sci.*, **20**, 637–649, [https://doi.org/10.1016/0272-7714\(85\)90112-X](https://doi.org/10.1016/0272-7714(85)90112-X).
- Pein, J., A. Valle-Levinson, and E. V. Stanev, 2018: Secondary circulation asymmetry in a meandering, partially stratified estuary. *J. Geophys. Res. Oceans*, **123**, 1670–1683, <https://doi.org/10.1002/2016JC012623>.
- Ralston, D. K., and M. T. Stacey, 2005a: Longitudinal dispersion and lateral circulation in the intertidal zone. *J. Geophys. Res.*, **110**, C07015, <https://doi.org/10.1029/2005JC002888>.
- , and —, 2005b: Stratification and turbulence in subtidal channels through intertidal mudflats. *J. Geophys. Res.*, **110**, C08009, <https://doi.org/10.1029/2004JC002650>.
- , G. W. Cowles, W. R. Geyer, and R. C. Holleman, 2017: Turbulent and numerical mixing in a saltwedge estuary: Dependence on grid resolution, bottom roughness, and turbulence closure. *J. Geophys. Res. Oceans*, **122**, 692–712, <https://doi.org/10.1002/2016JC011738>.
- Rozovskii, I. L., 1957: *Flow of Water in Bends of Open Channels*. Academy of Sciences of the Ukrainian SSR, 233 pp.
- Scully, M. E., W. R. Geyer, and J. A. Lerczak, 2009: The influence of lateral advection on the residual estuarine circulation: A numerical modeling study of the Hudson River Estuary. *J. Phys. Oceanogr.*, **39**, 107–124, <https://doi.org/10.1175/2008JPO3952.1>.
- Seim, H. E., and M. C. Gregg, 1997: The importance of aspiration and channel curvature in producing strong vertical mixing over a sill. *J. Geophys. Res.*, **102**, 3451–3472, <https://doi.org/10.1029/96JC03415>.
- Shchepetkin, A. F., and J. C. McWilliams, 2005: The Regional Oceanic Modeling System (ROMS): A split-explicit, free-surface, topography-following-coordinate oceanic model. *Ocean Modell.*, **9**, 347–404, <https://doi.org/10.1016/j.ocemod.2004.08.002>.
- Simpson, J., and R. Nunes, 1981: The tidal intrusion front: An estuarine convergence zone. *Estuarine Coastal Shelf Sci.*, **13**, 257–266, [https://doi.org/10.1016/S0302-3524\(81\)80024-2](https://doi.org/10.1016/S0302-3524(81)80024-2).
- , and P. Linden, 1989: Frontogenesis in a fluid with horizontal density gradients. *J. Fluid Mech.*, **202**, 1–16, <https://doi.org/10.1017/S0022112089001072>.
- Simpson, J. H., J. Brown, J. Matthews, and G. Allen, 1990: Tidal straining, density currents, and stirring in the control of estuarine stratification. *Estuaries*, **13**, 125–132, <https://doi.org/10.2307/1351581>.
- Smith, R., 1982: Where to put a steady discharge in a river. *J. Fluid Mech.*, **115**, 1–11, <https://doi.org/10.1017/S0022112082000615>.
- Soulsby, R., 1990: Tidal current boundary layers. *Ocean Engineering Science*, B. Le Méhauté and D. M. Hanes, Eds., *The Sea—Ideas and Observations on Progress in the Study of the Seas*, Vol. 9B, John Wiley & Sons, 523–566.
- Stacey, M. T., J. R. Burau, and S. G. Monismith, 2001: Creation of residual flows in a partially stratified estuary. *J. Geophys. Res.*, **106**, 17 013–17 037, <https://doi.org/10.1029/2000JC000576>.
- , T. Rippeth, and J. D. Nash, 2011: Turbulence and stratification in estuaries and coastal seas. *Treatise on Estuarine and Coastal Science*, E. Wolanski and D. S. McLusky, Eds., Elsevier, 9–35.
- Sternberg, R., 1968: Friction factors in tidal channels with differing bed roughness. *Mar. Geol.*, **6**, 243–260, [https://doi.org/10.1016/0025-3227\(68\)90033-9](https://doi.org/10.1016/0025-3227(68)90033-9).
- Thomson, J., 1877: V. On the origin of windings of rivers in alluvial plains, with remarks on the flow of water round bends in pipes. *Proc. Roy. Soc. London*, **25**, 5–8, <https://doi.org/10.1098/RSPL.1876.0004>.
- Umlauf, L., and H. Burchard, 2003: A generic length-scale equation for geophysical turbulence models. *J. Mar. Res.*, **61**, 235–265, <https://doi.org/10.1357/002224003322005087>.
- Valle-Levinson, A., 2008: Density-driven exchange flow in terms of the Kelvin and Ekman numbers. *J. Geophys. Res.*, **113**, C04001, <https://doi.org/10.1029/2007JC004144>.
- , 2011: Large estuaries (effects of rotation). *Treatise on Estuarine and Coastal Science*, E. Wolanski and D. McLusky, Eds., Academic Press, 123–139.
- Warner, J. C., C. R. Sherwood, H. G. Arango, and R. P. Signell, 2005: Performance of four turbulence closure models implemented using a generic length scale method. *Ocean Modell.*, **8**, 81–113, <https://doi.org/10.1016/j.ocemod.2003.12.003>.
- , —, R. P. Signell, C. K. Harris, and H. G. Arango, 2008: Development of a three-dimensional, regional, coupled wave, current, and sediment-transport model. *Comput. Geosci.*, **34**, 1284–1306, <https://doi.org/10.1016/j.cageo.2008.02.012>.

- , B. Armstrong, R. He, and J. B. Zambon, 2010: Development of a Coupled Ocean–Atmosphere–Wave–Sediment Transport (COAWST) modeling system. *Ocean Modell.*, **35**, 230–244, <https://doi.org/10.1016/j.ocemod.2010.07.010>.
- , W. R. Geyer, D. K. Ralston, and T. Kalra, 2020: Using tracer variance decay to quantify variability of salinity mixing in the Hudson River Estuary. *J. Geophys. Res. Oceans*, **125**, e2020JC016096, <https://doi.org/10.1029/2020JC016096>.
- Warner, S. J., and P. MacCready, 2014: The dynamics of pressure and form drag on a sloping headland: Internal waves versus eddies. *J. Geophys. Res. Oceans*, **119**, 1554–1571, <https://doi.org/10.1002/2013JC009757>.